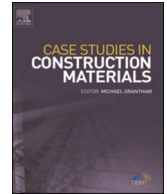




ELSEVIER

Contents lists available at [ScienceDirect](https://www.sciencedirect.com)

Case Studies in Construction Materials

journal homepage: www.elsevier.com/locate/cscm

Mechanical behavior of a new type of reinforced concrete composite slab with a joint

Feng Lou^{a,b,c}, Xiulong Chen^{a,b,*}, Bin Luo^{a,b}, Zhong Chen^c

^a Key Laboratory of Concrete and Prestressed Concrete Structures of the Ministry of Education, Southeast University, Nanjing 211189, China

^b School of Civil Engineering, Southeast University, Nanjing 211189, China

^c Zhejiang Dadongwu Construction Science & Technology Co., LTD, Huzhou 313017, China

ARTICLE INFO

Keywords:

Composite slab
Bearing capacity
Flexural behavior
Four-point bending test
Numerical analysis

ABSTRACT

Composite slabs, consisting of a precast plank and a cast-in-situ concrete topping, are the most commonly used horizontal structural components in prefabricated buildings. In order to solve the problem that the precast plank of composite slab is easy to crack and a lot of vertical supports are needed in its construction, this study proposes a new type of composite slab with a joint. The precast plank of this novel composite slab is fully prefabricated in the midspan area, and concrete is poured on-site only at the surrounding joints. In this paper, the bending performance of three composite slabs with a joint in different shapes of concrete topping and one cast-in-situ slab was investigated. The test results showed that the novel composite slabs with a joint in T-shape and trapezoidal concrete topping had similar properties as the cast-in-situ slab, including bearing capacity and cracking load, which can meet practical requirement. The use of bent-up steel bars and roughening of the interface between the precast plank and topping concrete can ensure effective transmission of internal forces at joint. The bearing capacity of the composite slabs with a joint in T-shape and trapezoidal concrete topping was evaluated using the formula in GB50010–2010, and the experimental values were 1.06 and 1.1 times the theoretical values, respectively, which provides a foundation for the design of two types of composite slabs with a joint. Meanwhile, based on the FEA software ABAQUS, numerical simulation was conducted on the composite slab with a joint in T-shaped concrete topping. The numerical finding exhibit close agreement with experimental results in terms of load-midspan deflection curve and the crack distribution.

1. Introduction

Precast concrete (PC) structures can be seen in buildings throughout the world due to its advantage of better construction quality, lower labor costs, and shorter construction times [1]. Composite slab, as one of the most commonly used elements in floor systems of PC residential buildings, is formed by bottom precast planks and a cast-in-situ concrete topping. In order to improve the flexural stiffness of the bottom precast plank and increase the bonding performance between the precast plank and the cast-in-situ concrete topping, lattice girders are usually installed in the precast plank. However, due to the limitation of the thickness of the composite slab

* Corresponding author at: Key Laboratory of Concrete and Prestressed Concrete Structures of the Ministry of Education, Southeast University, Nanjing 211189, China.

E-mail address: chenxiulong@seu.edu.cn (X. Chen).

<https://doi.org/10.1016/j.cscm.2023.e02773>

Received 27 September 2023; Received in revised form 23 November 2023; Accepted 8 December 2023

Available online 9 December 2023

2214-5095/© 2023 The Author(s). Published by Elsevier Ltd. This is an open access article under the CC BY-NC-ND license (<http://creativecommons.org/licenses/by-nc-nd/4.0/>).

with lattice girders used in China, the height of the lattice girder is usually small [2]. As a result, the improvement in stiffness of the precast plank by the lattice girder is limited, which requires the erection of vertical supports during the construction process, increasing the construction cost and prolonging the construction period [3]. Therefore, it is very necessary to propose a composite slab that can achieve unsupported construction.

Some improvement measures have been proposed to reduce the use of vertical supports in the construction process of composite slabs. Wu et al. [4] set a detachable truss rib on the bottom of the precast plank to replace the vertical support, realizing the construction without vertical support and improving the crack resistance of the slab. The truss rib that was placed at the bottom of the precast plank can be reused, but it is inconvenient to remove it. Moreover, based on the concept of a steel-concrete composite structure, measures such as concrete ribs and steel ribs were set on top of the precast plank can effectively improve its bending performance [5–7]. In addition to the above measures, good results have also been achieved by using grout steel tube, special materials, or components. Hou et al. [8] proposed a new type of composite slab with grouted-round-steel tube truss and conducted bending tests on it. The test results indicate that this type of composite slab has good ductility and can meet construction requirements. Ou et al. [9] investigated the flexural performance of composite slabs made of crumb rubber concrete or conventional concrete. They discovered that the bearing capacity and end-slippage of composite slabs made of crumb rubber were equivalent or even better than those made of the conventional concrete. Erfan et al. [10] conducted numerical simulations on concrete beams strength with FRP materials and found that using CFRP sheets to reinforce concrete beams can effectively improve their bearing capacity and prevent crack propagation. Maedeh et al. [11] conducted bending tests on concrete beams with steel reinforcement and a hybrid usage of GFRP reinforcement with varying fiber ratios, respectively. They concluded that concrete beams using 1.5% polypropylene fibers and GFRP rebars can reach the same bending strength as concrete beams using steel bars. Wang et al. [12] proposed a novel bamboo-concrete composite beam with precast lightweight concrete slab. Shear test results indicated that this new type composite slab had a similar shear strength but a higher stiffness than the cast-in-situ bamboo-lightweight concrete composite slab. However, the composite slabs mentioned above have a large amount of concrete poured on site and a low assembly rate.

In addition, considering that in practical engineering, the floor usually requires multiple precast planks to be spliced together due to the limitation of the size of the precast plank. Hence, for the proposal of a new type of composite slab, the following two key points need to be considered. 1) The connection joint can effectively and continuously transmit force. 2) The interface between the precast plank and the cast-in-situ concrete topping should have sufficient bonding performance.

The current T/CECS 715–2020 [13] provides three types of joints between the precast plank: monolithic connection with post-pouring strip, separated monolithic connection without gap, and monolithic connection without gap, as shown in Fig. 1. Some scholars have done experimental research on the composite slab connected with joints. Ye et al. [14] carried out the four-point flexural tests on two composite slabs connect by post-pouring strip joints and two cast-in-situ slabs. The results indicated that by strengthening the reinforcement at the joint or changing the relative position of the bottom longitudinal reinforcements to increase the effective cross-sectional height, the joint can effectively transmit internal force. Ding et al. [15] optimized the joint configuration of composite slabs with post-pouring strip joints and found that the bending performances of the new type of composite slab with joints were basically consistent with the cast-in-situ slab through experimental tests. Zhang et al. [16] performed experiments on two-way composite slabs connected without gap. The results showed that the effective transmission of moment can be achieved through measures such as strengthening additional rebar and densifying lattice girder at the joint connection. However, the joint without gap can cause the flexural stiffness of the slabs in the vertical joint direction to be slightly less than that in the parallel joint direction. Liu et al. [17] tested the mechanical performance of composite slabs with a joint and found that the bearing capacity of the composite slab connected without a gap could be improved by changing the arrangement of rebars. Xiao et al. [18] conducted bending tests on a cast-in-situ slab and a composite slab with lattice girder connected by a post-pouring stripe. The conclusion validated that the bending behavior of the composite slab connected by the post-pouring strip joint was similar to those of the traditional cast-in-situ slab. Overall,

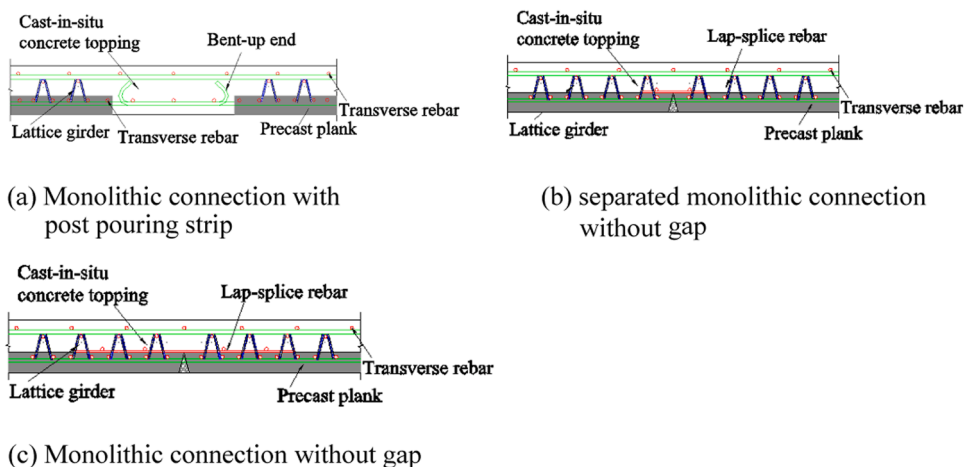


Fig. 1. Types of joints for LGSS [13].

the joint with the post-pouring strip has better integrity compared to the joint without gap, and can better meet the force transmission requirements of the composite slab.

On the other hand, some scholars have conducted studies on the bonding behavior between the precast plank and the cast-in-situ concrete topping. Sifan et al. [19] studied the flexural behavior of the composite slabs with different interface treatment methodologies on the interface. It was concluded that rough machining of the interface in the transverse direction using a steel wire brush is an effective method to ensure adequate bonding of the interface. Lam et al. [20] evaluated the bonding performance of composite slab and found that there is sufficient bonding at the interface, even without rebar passing through the interface. Adawi et al. [21,22] presented investigations on the flexural behavior of composite hollow core slabs. The results verified that the shear strength of the interface roughened by machines can meet the requirements of North American design codes. Ibrahim et al. [23] performed experiments on precast hollow core slabs and validated that rough surface conditions would enhance the shear resistance of the hollow core slabs, which was consistent with the conclusion drawn by Girhammar, et al. [24]. As mentioned above, by roughening the surface of the precast plank, good bonding properties of the interface can be achieved.

Based on the above research results and referring to the technical specification for prefabricated concrete structures (JGJ1–2014), this study proposes a new type of composite slab with a joint. Its characteristics are full section prefabrication in the mid span area of the precast plank, and partial prefabrication in the surrounding joint area. This new type of composite slab can not only achieve unsupported construction but also reduce the amount of concrete pouring on site, and the precast plank can serve as a worktable. In order to determine the reasonable configuration of this new type of composite slab with a joint, a total of four slabs were produced and tested under four-point bending load, including one cast-in-situ slab and three new types of composite slabs with a joint in different shape of concrete topping. The cracking load, crack distribution, and ultimate bearing capacity were analyzed. In addition, numerical simulation of laminated plate specimens was conducted based on the finite element analysis software ABAQUS, and the accuracy of finite element analysis was verified by comparing it with experimental results, providing a foundation for subsequent research.

2. Experimental investigation

2.1. Specimen design and preparation

In this study, four slabs were prepared and tested, including one cast-in-situ slab and three composite slabs. For all specimens, the length, width, and thickness were 3980 mm, 960 mm, and 120 mm, respectively. The geometric characteristics of specimens are shown in Table 1. Using the following rules to name the specimens: CS represents the cast-in-situ RC slab; SS-1, SS-2, and SS-3 represent the composite slabs with a joint in shape of T-shaped, trapezoidal, and rectangular cast-in-situ concrete topping, respectively. The geometrical dimensions and steel bars arrangement as shown in Fig. 2 and Fig. 3. For specimen CS, mesh reinforcement was composed of steel bars with a diameter of 8 mm and a spacing of 150 mm. The composite slabs are formed by connecting two precast planks through cast-in-situ topping concrete. Seven D8 longitudinal steel bars were respectively placed at the bottom and top of the precast plank with a 15 mm concrete cover. The longitudinal steel bars extend a certain length out of the precast plank, and the bottom steel bars have a 135° bend-up to be embedded in the cast-in-situ concrete topping. The transverse steel bars used in precast plank were D8 at a spacing of 150 mm. The arrangement of steel bars at the concrete topping can be seen in Fig. 3.

The production of composite slabs required pouring concrete twice in sequence. The specific production process was as follow: (1) Pouring concrete into the formwork with the mesh reinforcement to manufacture the precast plank. (2) The surface of the precast plank was roughened in the transverse direction with a wire brush in order to improve the bond performance between the precast plank and the topping concrete. (4) After the curing of the precast plank was completed, the longitudinal steel bars at the joint of the two precast planks were connected, and the transverse steel bars were placed. Finally, the cast-in-situ topping was poured with concrete. Taking specimen SS-1 as an example, the production process is shown in Fig. 4.

2.2. Material property

The material properties of steel bars used in slabs are displayed in Table 2, which were obtained from the axial compression test of three specimens according to GB/T 228.1–2010 [25]. The axial compressive strengths of the concrete were measured in accordance with the requirements of GB/T 50081–2019 [26] using standard 150 mm × 150 mm × 150 mm cubes. The measured axial compressive strengths of the precast plank and the cast-in-situ concrete topping were shown in Table 3, respectively.

Table 1
Specimen design specifications.

Specimen	Length/mm	Width/mm	Overall slab height/mm	Shape of cast in place layer	Spacing of precast plank /mm
CS	3980	960	120	-	300
SS-1	3980	960	120	Letter T-shaped	300
SS-2	3980	960	120	Trapezoidal shape	300
SS-3	3980	960	120	Rectangular shape	300

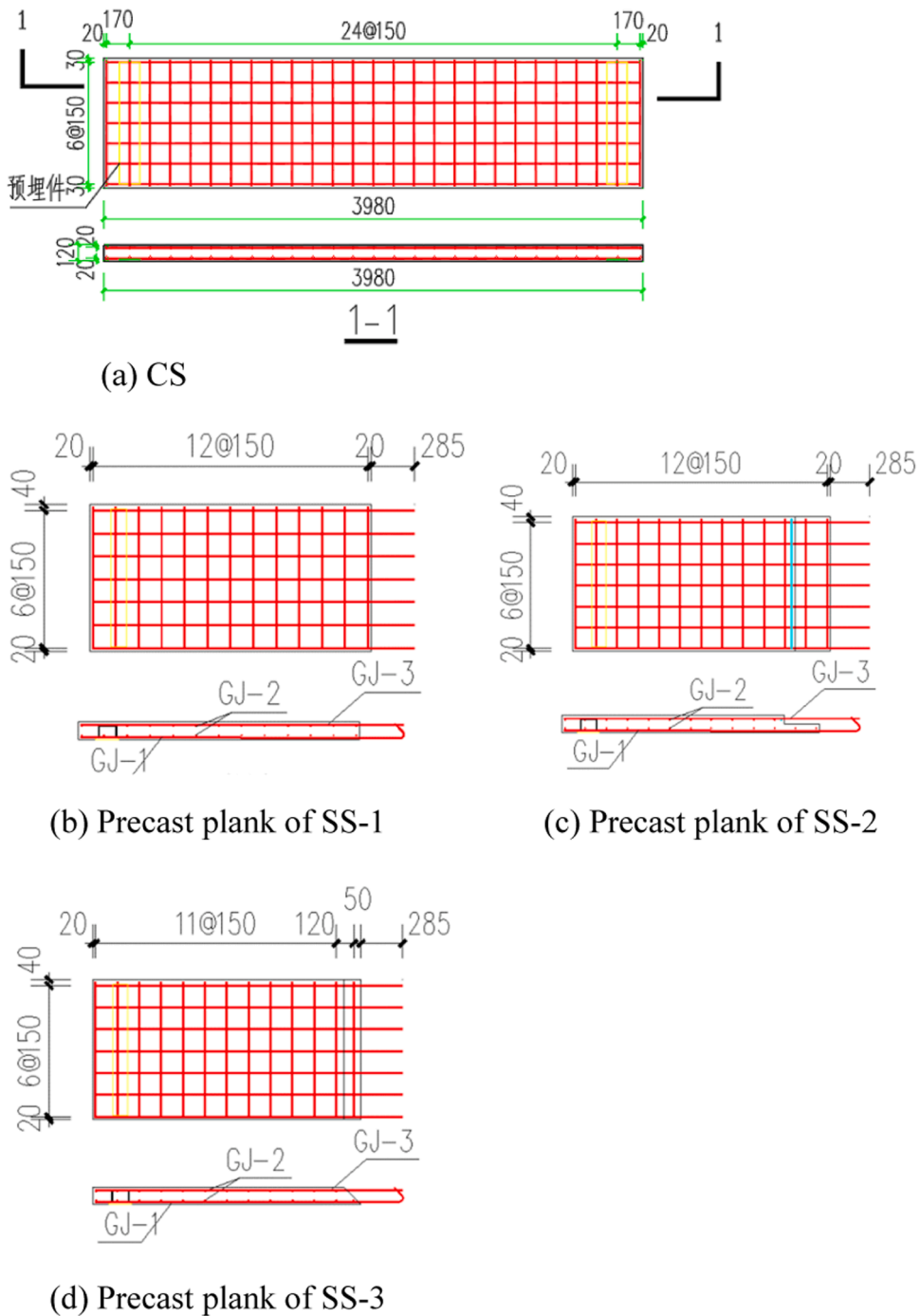


Fig. 2. Geometrical dimensional and steel bars arrangement of specimen CS (unit:mm).

2.3. Testing setups and procedures

The loading device used for conducting the bending test is shown in Fig. 5. As shown in Fig. 5, One end of the specimen was a fixed hinge support, and the other end was a sliding hinge support. The application of monotonic load was achieved through a jack with a measuring rang of 1000 kN. The transfer girders were located on two rollers, which were placed at 500 mm on both sides of the midspan. This led to the formation of a constant moment region of 1000 mm at the midspan. In order to analyze the strain development of steel bars under bending load, 10 strain gauges were glued to steel bars and concrete with epoxy resin adhesive, and the specific locations of the strain gauges are detailed in Section 3.3. A linear variable displacement transducers were installed at the

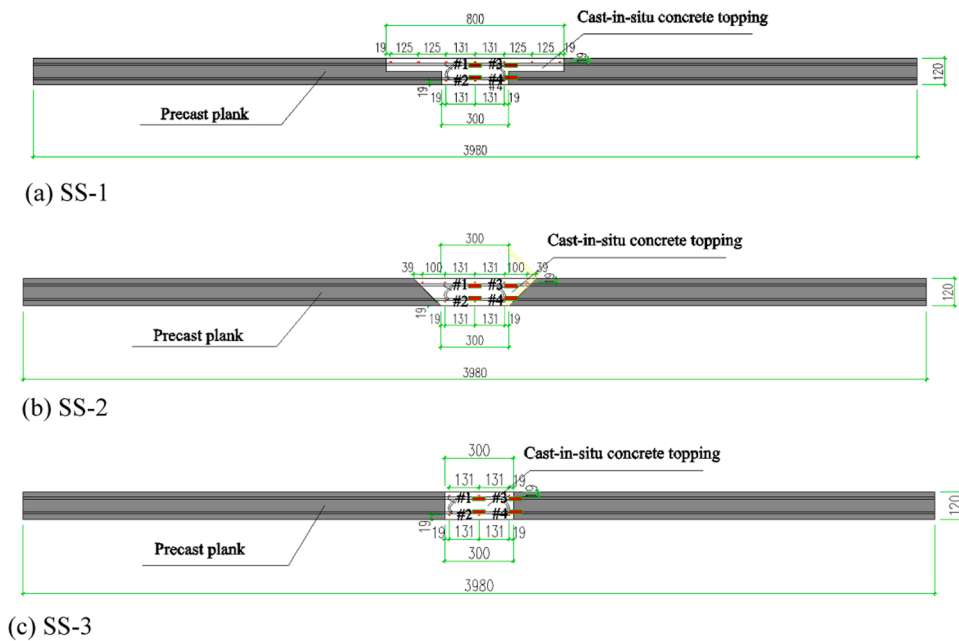


Fig. 3. Design detail of composite slabs with a joint.

midspan position of the bottom surface to record the deflection.

In this test, loading was carried out by controlling the force, and the specific loading process was as follows: Firstly, three cycles of preloading were performed on the slab, with a preloading value of 2 kN, to check whether the data acquisition instrument could work normally. Then, the applied load was gradually increased in increments of 2 kN. When the first crack occurs on the slab, the load increment was changed to 4 kN. After each increment of loading was completed, maintain it for 10 min to allow concrete cracks to develop. The test was terminated until the specimen failed.

3. Testing results

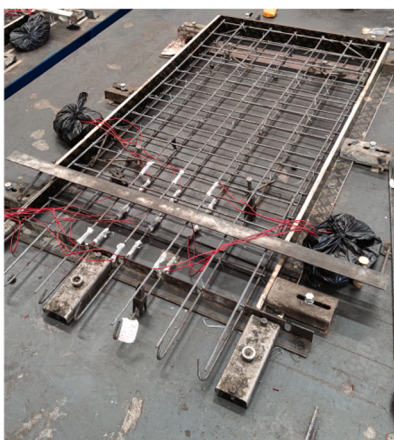
3.1. Crack pattern

The failure modes of slabs are presented in Fig. 6. It can be seen from Fig. 6, all specimens exhibit typical flexural ductile failure. For example, the first crack of all specimens appears in the constant bending moment zone at the bottom surface of the slab. The first cracking loads of specimens CS (9 kN) and SS-2 (9.3 kN) were bigger than that of specimen PS-1 (8.8 kN) and PS-3 (4.7 kN). As the applied load increases, more transverse cracks appeared in the constant bending moment zone and gradually extended to the side surface of the slab. Fig. 7 depicts the distribution of bottom surface cracks after loading was completed. As shown in Fig. 7, it can be seen that the bottom interface of specimen SS-2 did not crack during the loading process, indicating better integrity compared to specimen SS-1 and SS-3. It should be noted that, for all composite slabs, there was no obvious tearing or significant sliding on the interface. This indicates that the precast plank and concrete topping have good collaborative work ability.

3.2. Load – midspan deflection behavior

Fig. 8 compares the load-midspan deflection curves of the cast-in-situ slab and composite slabs. According to the development characteristics of the curve, it was divided into three phase. (I) Elastic loading stage, where the midspan deflection presents a linear relationship with the applied load, and the concrete did not crack. (II) Cracking stage, where the transverse cracks appear in the tension area, resulting in a decrease in bending stiffness, and the curve is still approximately linear development. (III) Yielding stage, where the load-midspan deflection curves appears an obvious inflection point as the tensile steel bars exceeded the yield strain, and the midspan deflection increases rapidly with the increase of load.

Table 4 summarizes the representative values of the load-midspan deflection curve, including first cracking load P_{cr} , yield load P_y , ultimate bearing capacity P_u , and corresponding midspan deflection. The first cracking load was identified through observation according to the method specified in GB/T 50152–2012 [27]. The yield load was obtained from the readings of the strain gauges attached to the longitudinal steel bars. For the determination of the ultimate bearing capacity, according to GB/T 50152–2012 [27], when the specimen reaches one of the following characteristics, it is considered that the specimen has undergone bending failure and reached its ultimate bearing capacity. a) The midspan deflection of the slab reaches 1/50 of the span. b) The width of the concrete crack at the bottom of the slab reaches 1.50 mm, or the strain of the tensile reinforcement exceeds 0.01. c) Cracking and crushing of concrete in the



(a) Setting formwork



(b) Pouring concrete to form the precast plank.



(c) Pouring concrete topping

Fig. 4. Production of the specimen SS-1.

Table 2

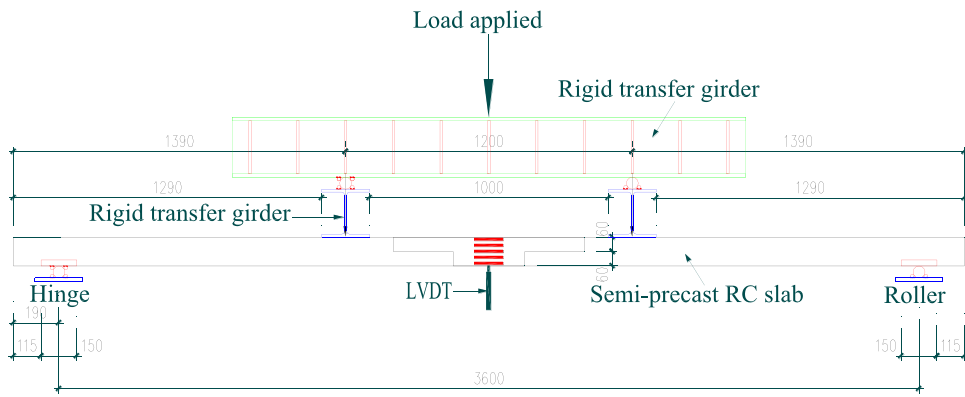
Material properties of steel bars.

Member	No.	Diameter d (mm)	Elastic modulus E_s (GPa)	Yielding strength f_y (MPa)	Ultimate strength f_u (MPa)
steel bars	1	8	19.6	524	688
	2	8	19.2	520	675
	3	8	19.7	528	690

Table 3

Material properties of the concrete.

concrete	No.	Compressive strength/MPa	Average compressive strength/(MPa)	Elastic modulus/(GPa)	Average elastic modulus/(GPa)
Precast plank	1	38.3	38.5	32.2	32.2
	2	39.2		32.4	
	3	38.0		32.1	
Cast-in-situ concrete topping	4	46.6	46.7	34.0	34.0
	5	46.2		33.9	
	6	47.3		34.1	



(a) Schematic diagram. (units: mm)



(b) Test setup

Fig. 5. The loading device for bending test.

compression zone. It can be seen from Table 3 that the ultimate bearing capacity of specimen SS-1 is 28.0 kN, which is similar to the 28.1 kN of specimen CS. The bearing capacity of the SS-2 is 29.8 kN, which is 6% higher than that of the CS. However, compared with CS, the cracking load and bearing capacity of SS-3 were decreased by 47% and 11%. Overall, the bending performance of specimen SS-1 and SS-2 is similar to that of cast-in-place slab CS, both of which are better than specimen SS-3.

3.3. strain response of the steel bars and concrete

Fig. 9. shows the strain development of longitudinal steel bars at the top and bottom of the slab. The specific layout position of the strain gauge is depicted in Fig. 3. When the strain of the steel bar reaches about $2670 \mu\epsilon$, it indicates that the steel bar has yielded. Due to the damage of the #2 strain gauges of specimen SS-2 and SS-3 during the pouring of concrete, the strain at the corresponding position could not be collected. As displayed in Fig. 9, the strain of the steel bars at the gauging point #2 and #4 of the cast-in-site slab specimen yielded almost simultaneously, while for the composite slab SS-1, the steel bars at the gauging point #4 yielded, and the longitudinal steel bars at the gauging point #2 did not reach the yield strain. This is attributed to the overlapping steel bars at the midspan of the composite slab specimen, resulting in a decrease in steel bar stress.

Fig. 10 (a) ~ (d) shows the strain development at different heights on the side surface of the specimens CS, SS-1, SS-2, and SS-3. #a~#e were concrete measurement points arranged from top to bottom on the side surface, as shown in Fig. 5. As depicted in Fig. 10 (a) ~ (d), the strain of concrete followed a linear distribution pattern along the height direction of the cross-section. The strain

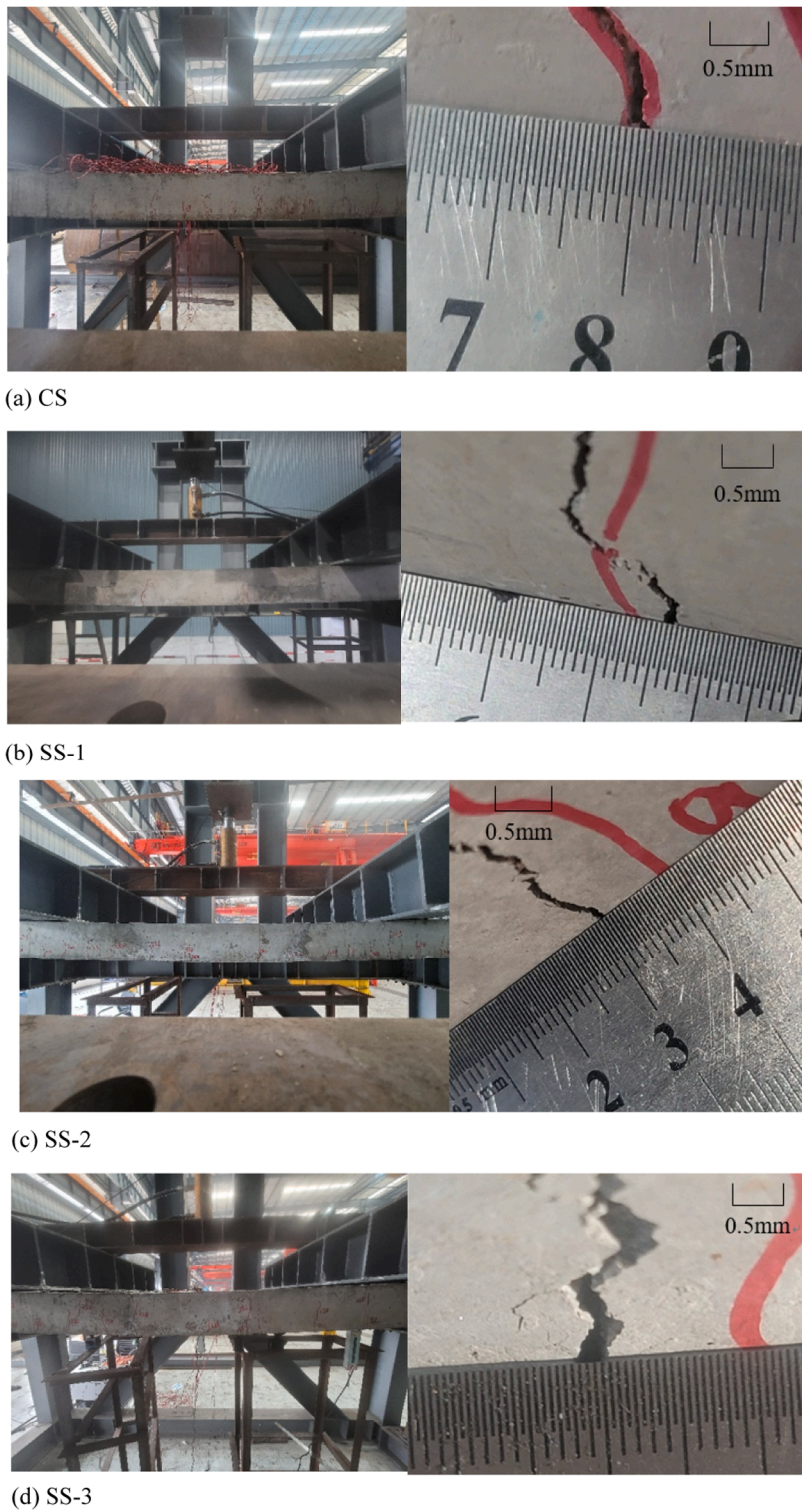


Fig. 6. Failure modes of the slabs.

development at the bottom of the cast-in-situ slab specimen CS is faster than that of the composite slab specimens. Fig. 10 (e) compares the strain of the midspan concrete at the top of specimens CS, SS-1, SS-2, and SS-3. As shown in Fig. 10 (e), the midspan concrete at the top of all specimens has been in a compressive state, and the absolute value of strain increases with the increase of the applied load. The strain development of the cast-in-situ slab is significantly faster than that of composite slabs.

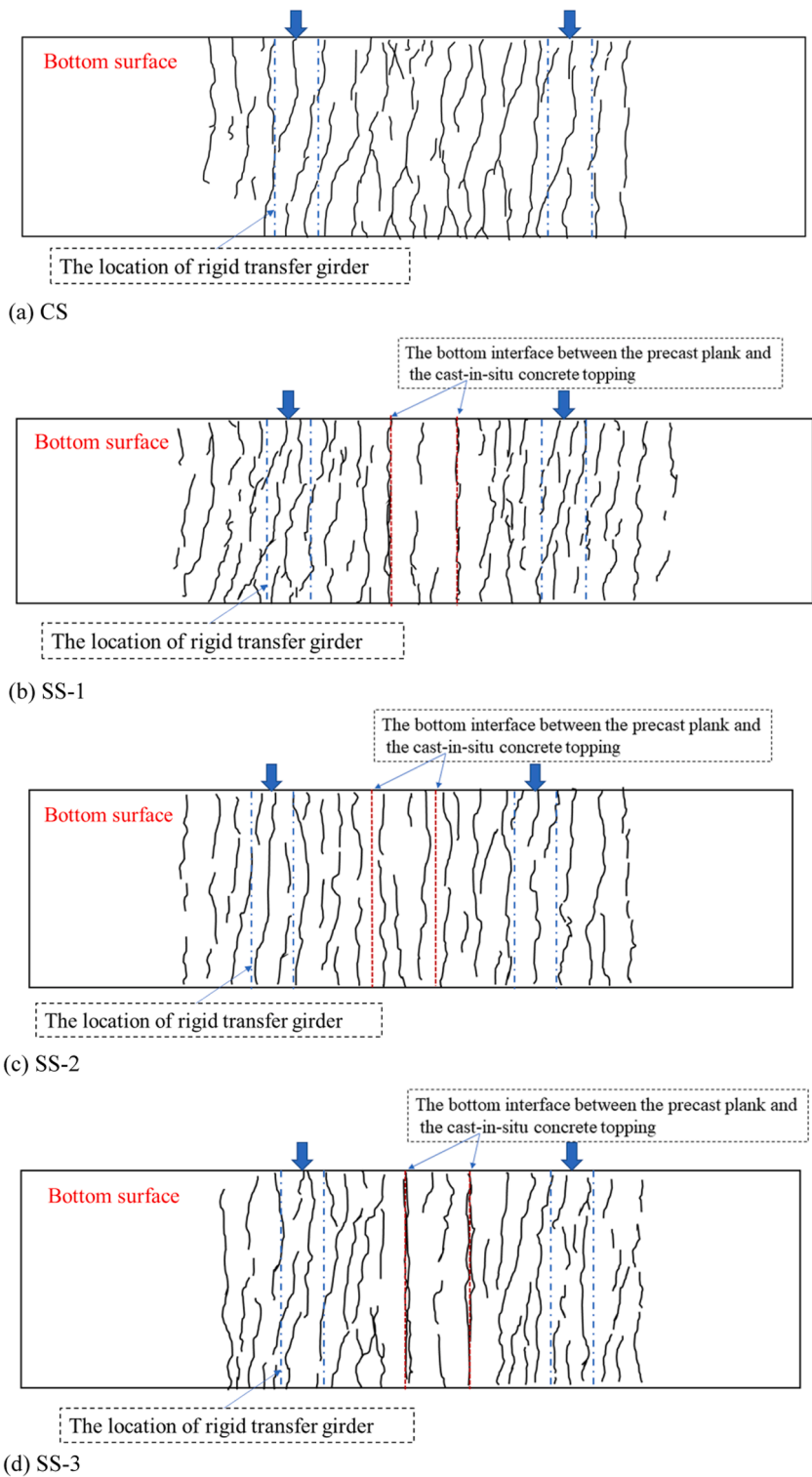


Fig. 7. Crack distributions in the bottom surface.

3.4. Calculation of bending bearing capacity

From the above experimental results, it can be seen that there is no relative slip of the interface for the three composite slabs, and their failure mode is bending failure, just like the cast-in-situ slab. Assuming that the cross-section of the composite slab conforms to

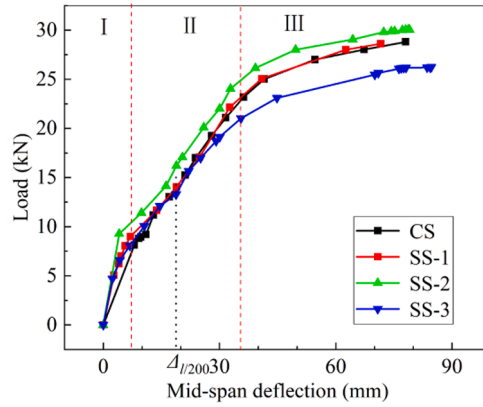


Fig. 8. Load-midspan deflection curve of slabs.

Table 4
Experimental values of representative point.

Specimen	First cracking point		Yield point		Ultimate point		Theoretical value of ultimate load	
	P_{cr}/kN	Δ_{cr}/mm	P_y/kN	Δ_y/mm	P_u/kN	Δ_u/mm	$P_{u,c}$	$P_u/P_{u,c}$
CS	9.0	9.8	23.1	36.1	28.1	67.2	25.8	1.09
SS-1	8.8	6.5	22.1	32.6	28.0	62.6	25.8	1.09
SS-2	9.3	4.1	24.0	32.8	29.8	72.0	25.8	1.16
SS-3	4.7	2.3	21.0	35.5	24.9	60.5	25.8	0.97

the assumption of a flat section, without considering the tensile strength of the concrete. According to the code for design of concrete structures GB50010–2010 [28], the flexural bearing moment of the normal section of concrete member is defined according to Eq. (1).

$$M_u = \alpha_1 f_c b x \left(h_0 - \frac{x}{2} \right) \tag{1}$$

Parameter x is calculated according to Eq. (2), where f_y is the yield strength of longitudinal steel bar; A_s is the cross-sectional area of longitudinal reinforcement in the tensile zone; f_c is the axial tensile strength of concrete; b is the width of the rectangular section.

$$x = \frac{f_y A_s}{\alpha_1 f_c b} \tag{2}$$

In Eq. (1), h_0 is the effective height of the section. The default value of the ratio α_1 is 1.0, according to GB50010–2010[28].

According to the above calculation method and structural mechanics, the ultimate loads $P_{u,c}$ corresponding to the ultimate bending moments of the composite slab with joint and the cast-in-situ slab were calculated separately. The comparison between the measured and theoretical values of the ultimate load of the specimens is shown in Table 4. From Table 4, it can be seen that the measured values of the ultimate load of CS, SS-1, and SS-2 are greater than the theoretical values, and the measured values are approximately 1.09–1.16 times the theoretical values. It indicates that the joint form used in specimen SS-1 and SS-2 can effectively withstand bending moments and have sufficient safety reserves. However, for specimen SS-3, the measured ultimate bearing capacity is smaller than the theoretical value, and its bending performance is poorer than that of cast-in-situ slabs.

4. Finite element analysis

In order to further clarify the flexural behavior of the composite slab with a joint and supply a theoretical basis for further study, this section conducted numerical simulation of the specimen SS-1 using the nonlinear FEA software ABAQUS/Standard [29]. The modeling strategy was elaborated and the accuracy of finite element analysis was verified.

4.1. Models for mechanical behaviors of materials

ABAQUS provides smeared cracking model and plastic damage model to describe the material properties of concrete. The two models both can accurately simulate the flexural properties of the concrete members. Zhang et al. [30]. conducted numerical analysis of concrete composite slabs, and found that the plastic damage model can better simulate their mechanical properties. Therefore, the concrete damage plasticity (CDP) model was adopted to simulate the constitutive relationship of the concrete. The CDP model provided in ABAQUS describes the material properties of concrete by defining the uniaxial plasticity parameters, stress-inelastic strain relationship, and damage evolution under compression and tension. In this analysis, based on existing research results [31], the values

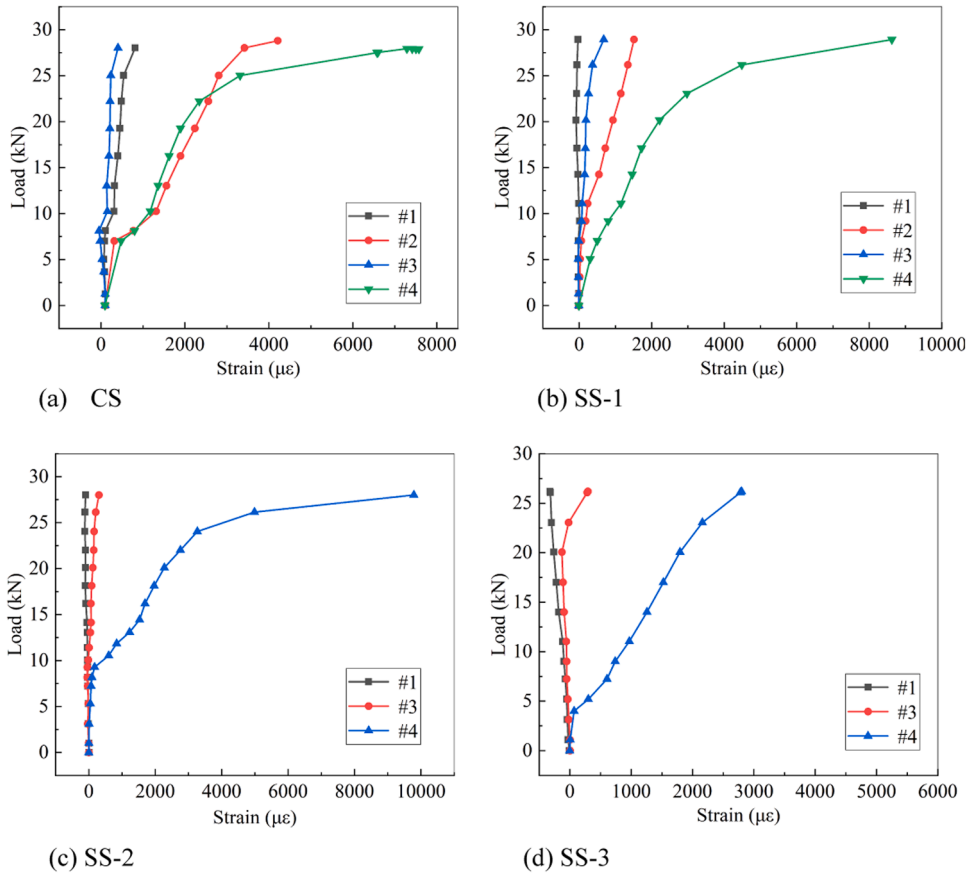


Fig. 9. Longitudinal strain of steel bar.

of the uniaxial plasticity parameters are summarized in Table 5. The empirical stress-inelastic strain curve of concrete was determined according to the GB50010–2010 [28]. Taking the precast plank as an example, the stress-strain relationship is shown in Fig. 11. For the damage evolution of concrete, Sidoroff. [32] proposed a calculation method for the damage factors, which can be directly inputted into the ABAQUS. The expressions of damage factors (D_t, D_c) are shown in Eq. (3).

$$D_t = 1 - \sqrt{\frac{\sigma_t}{E_c \epsilon_t}}; D_c = 1 - \sqrt{\frac{\sigma_c}{E_c \epsilon_c}} \quad (3)$$

As for the modeling of steel bar material properties, the multi-axial behavior (in both compression and tension) of steel bars was defined using an idealized bilinear curve [33], as shown in Fig. 12. It should point that the stress and corresponding strain obtained in Section 2.1 was converted into true stress and true strain according to Eq. (4) and filled in ABAQUS.

$$\epsilon_T = \ln(1 + \epsilon); \sigma_T = \sigma(1 + \epsilon) \quad (4)$$

4.2. Element type and mesh generation

In the FEM, the C3D8R element was used to model the components of concrete, supports, and loading plates, which has good calculation accuracy and was not prone to shear self-locking under bending load. As for steel bars, the T3D2 element was adopted. In order to balance the simulating accuracy and efficiency, the mesh size of the specimen was determined by a mesh sensitivity study. As show in Fig. 13, six layers of mesh were arranged along the slab thickness direction with the mesh size of 60 mm × 60 mm × 20 mm.

4.3. Contact interaction

The contact interaction exists between steel bars and concrete components, as well as between the precast plank and concrete topping. For the contact interaction between the steel bars and the concrete, all steel bars were embedded in the concrete, ignoring the relative sliding between the two. The interface properties of precast plank and concrete topping mainly include normal bond tensile and tangential bond shear. Both Coulomb-Friction model [34] and Cohesive model [34] can be used to describe this bonding property.

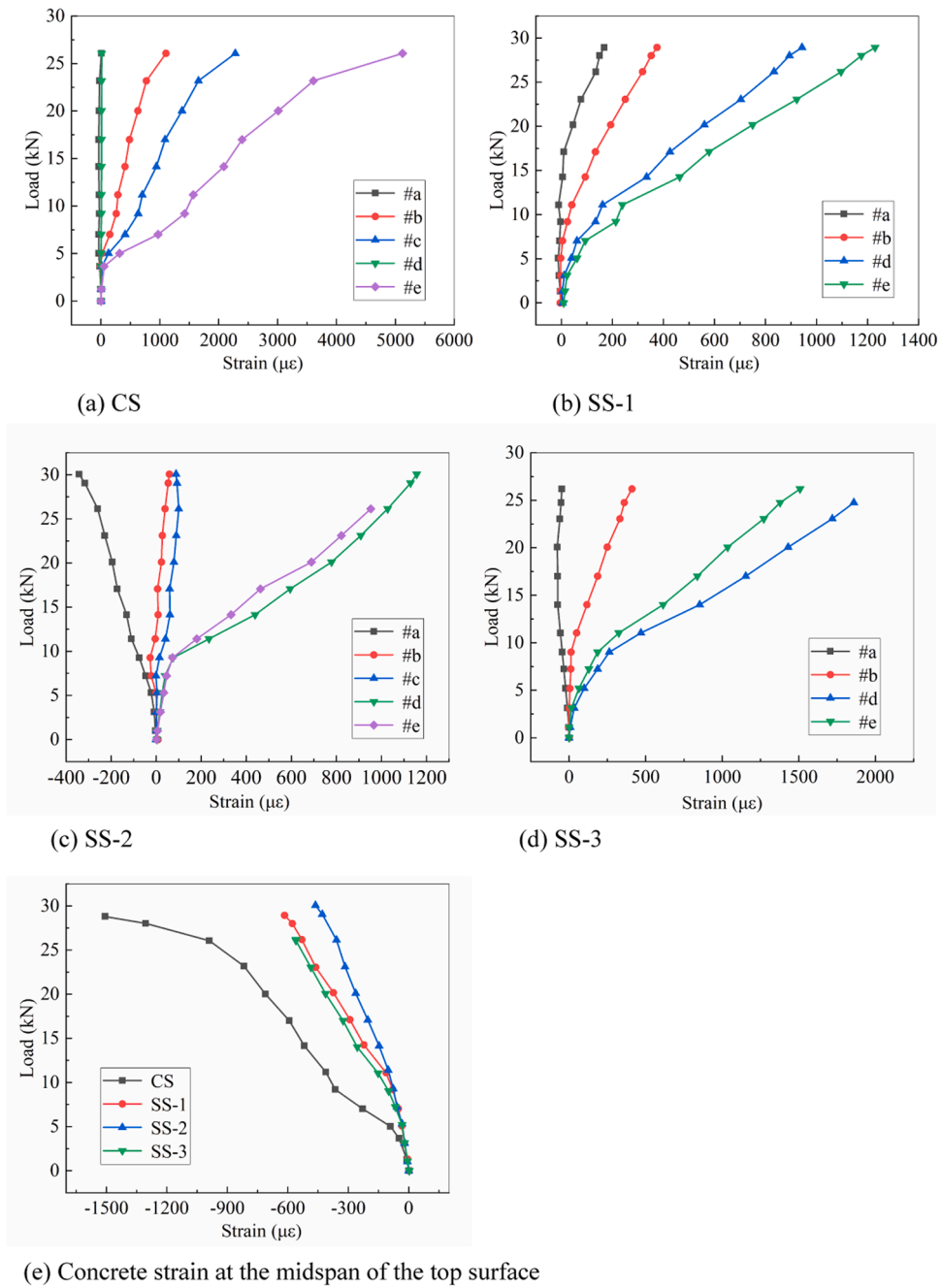


Fig. 10. Longitudinal strain of concrete.

Table 5
The values of plasticity parameters.

Plasticity parameters	The dilation angle in degree (ψ)	Flow potential eccentricity (ϵ)	Concrete biaxial-to-uniaxial cylinder compression strength ratio (f_{b0}/f_{c0})	The ratio of compressive to tensile meridians of the yield surface in deviatoric space (K_c)	Viscosity parameter
value	40°	0.1	1.16	0.6667	0.0005

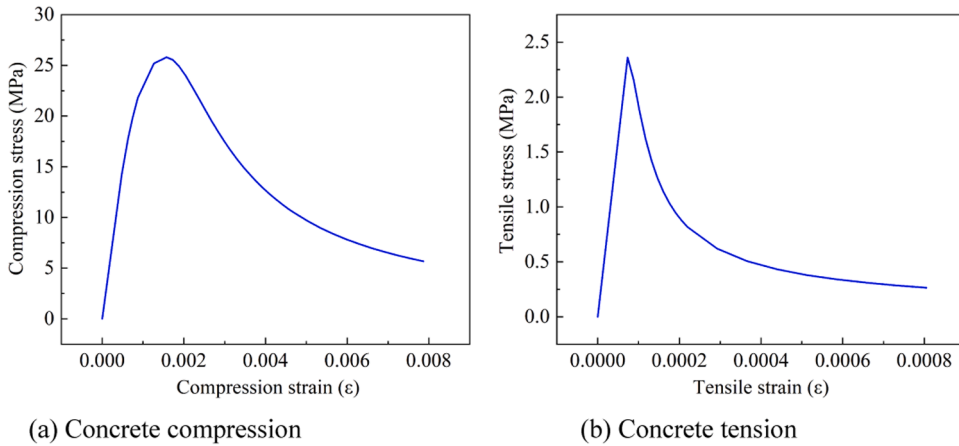


Fig. 11. Constitutive properties of concrete.

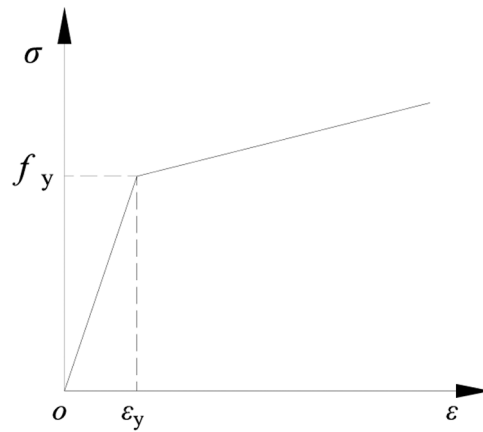


Fig. 12. Uniaxial stress-strain curve for steel bar.

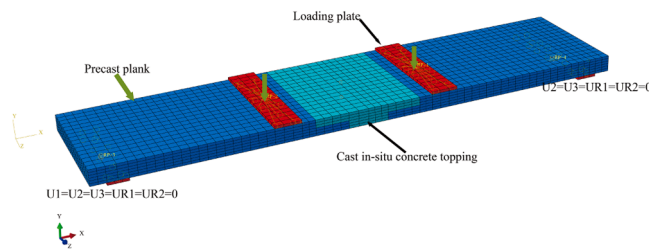


Fig. 13. The FEM of specimen SS-1.

4.3.1. Coulomb-Friction model

The shear stress-slip curve of the interface between the precast plank and topping concrete based on the coulomb friction model is shown in Fig. 14. The ABAQUS/Standard generally adopt the penalty stiffness method to define the frictional constraints, that is, it is considered that the interface can have finite elastic slip. As depicted in Fig. 14, τ_{crit} is the critical shear stress and its value is determined by μp , μ is the friction coefficient, p is the fraction of contact pressure. when shear stress is less than τ_{crit} , The interface is in the sticking friction (elastic) state, when shear stress is greater than τ_{crit} , it is in the slipping friction (plastic) state. In this study, the penalty function was adopted with a friction coefficient (μ) of 0.6 [35], and the shear stress (τ) limit was taken as 1.2 N/mm. The Coulomb friction model can only be used to describe the tangential shear properties of the interface. the normal direction can generally be defined as hard contact, that is, the interface can fully transfer compressive stress, and the tension can be set according to the demand for interface tension separation or non-separation.

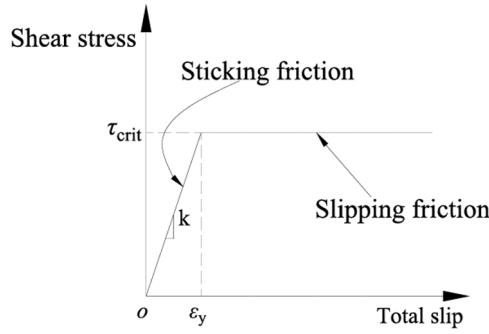


Fig. 14. Shear stress-slip curve of Coulomb friction model.

4.3.2. Cohesive model

The cohesive model provided by ABAQUS is mainly applied to simulate the cohesive action between two objects with negligible interface thickness. Due to its ability to define generalized stress-relative displacement constitutive equations in both normal and two tangential directions, it can be used to simulate the interface between new and old concrete. In addition, the model provides functions that are very similar to the cohesive elements defined using the law of traction-separation. However, the cohesion model is generally easier to define and allows for the simulation of a wider range of cohesive interactions. The relationship of traction and separation is shown in Fig. 15, including the linear elastic stage and damage decline stage. For the elastic behavior, it is defined according to Eq. (5).

$$\mathbf{t} = \begin{Bmatrix} t_n \\ t_s \\ t_t \end{Bmatrix} = \begin{bmatrix} K_{nn} & K_{ns} & K_{nt} \\ K_{ns} & K_{ss} & K_{st} \\ K_{nt} & K_{st} & K_{tt} \end{bmatrix} \begin{Bmatrix} \delta_n \\ \delta_s \\ \delta_t \end{Bmatrix} = \mathbf{K}\boldsymbol{\delta} \quad (5)$$

Where, \mathbf{K} denotes the elastic stiffness. $t_n, t_s,$ and t_t are the shear traction in three different direction, respectively. $\delta_n, \delta_s,$ and δ_t are the corresponding separations.

The damage decline stage consists of two ingredients: a damage initiation criterion and a damage evolution law. Damage initiation refers to the degradation of cohesive response at the contact point. When contact stress and/or contact separation meet certain specified damage initiation criteria, the degradation process begins. The criteria for determining the onset of damage in ABAQUS are as follows: maximum stress criterion, maximum separation criterion, quadratic stress criterion, and quadratic separation criterion. In this analysis, the maximum stress criterion was selected as the basis for damage initiation, this is, damage begins to develop when the maximum ratio of contact stress reaches a value of 1. The maximum stress criterion is determined by Eq. (6).

$$\max \left\{ \frac{t_n}{t_n^0}, \frac{t_s}{t_s^0}, \frac{t_t}{t_t^0} \right\} = 1 \quad (6)$$

Where $t_n^0, t_s^0,$ and t_t^0 are the peak values in three different directions, respectively.

The damage evolution in cohesive surface can be described as Eq. (7).

$$\begin{aligned} t_n &= \begin{cases} (1-D)\bar{t}_n, & \bar{t}_n \geq 0 \\ \bar{t}_n, & \bar{t}_n < 0 \end{cases} \\ t_s &= (1-D)\bar{t}_s, \\ t_t &= (1-D)\bar{t}_t \end{aligned} \quad (7)$$

where \bar{t} denotes the predicted contact stress, and the subscripts n, s, and t represent different directions, respectively.

To further reflect the damage evolution under a combination of three direction separations across the interface, an effective separation was proposed defined as Eq. (8).

$$\delta_m = \sqrt{\langle \delta_n \rangle^2 + \delta_s^2 + \delta_t^2} \quad (8)$$

In addition, when the damage evolution is defined, the plastic effective relative displacement $\delta_m^f - \delta_m^0$ should also be input, where δ_m^0 is the peak effective relative displacement and δ_m^f is the effective relative displacement during failure, or the energy consumed during interface failure G ($G^c = 1/2\delta^f t^0$) can be input.

In this analysis, the shear strength and constitutive properties of the interface were determined by referring to the test curve in reference. The cohesiveness model parameters [36] are shown in Table 6. The Coulomb-Friction model and Cohesive model were used for finite element analysis of specimen SS-1, respectively, and the results are shown in Section 4.5.

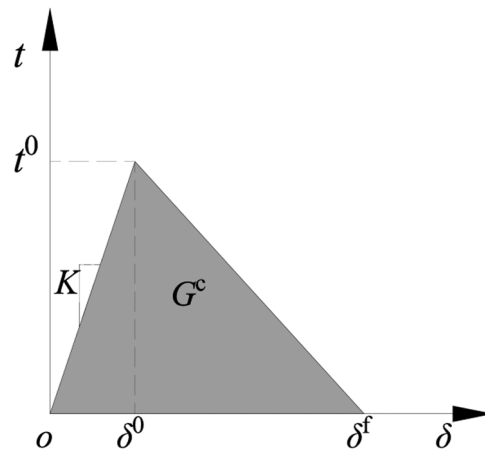


Fig. 15. Typical traction-separation response.

Table 6

Related parameters of Cohesive model.

Interaction property	Related parameter							
Cohesive model	Stiffness (MPa/mm)			Peak stress (MPa)				$\delta_m^f - \delta_m^0$ (mm)
	K_{nn}	K_{ss}	K_{tt}	t_n^0	t_s^0	t_t^0		
	100000	10	10	1.6	0.8	0.8	1	

4.4. Load and boundary conditions

The loads controlled by displacement were applied to the reference point (RP1, RP2), which were respectively coupled to the loading plates. Nonlinear static analysis using the Newton-Raphson iteration solution algorithm was adopted. The boundary conditions were applied to the reference point (RP3, RP4) which coupled with the support plate. For RP3, all translational degrees of freedom were constrained, and only the z-axis rotational degree of freedom was released. Only released the translational degrees of freedom of the x-axis and the rotational degrees of freedom of the z-axis of RP4, as shown in Fig. 13.

4.5. Verification of FEA results

The developed FEM was used to predict the flexural behavior of specimen SS-1. The failure modes and load-midspan deflection curves obtained from FEA were compared with the experimental test. Fig. 16 compares typical experimental and FEM load-midspan

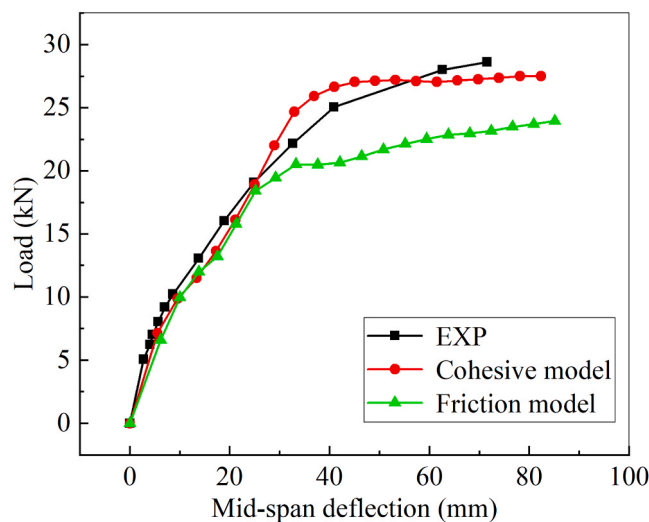


Fig. 16. Comparison of load-midspan deflection curves between the test and numerical result.

deflection responses of the slabs. As shown in Fig. 16, the load-midspan deflection curve obtained through numerical simulation using the cohesive force model was highly consistent with the experimental results, and the maximum error of the load discussed in Section 3.2 between the numerical result and the experimental result did not exceed 10%. Although, finite element simulation using Coulomb friction model can better simulate the mechanical properties of the composite slab before steel bars yielded, and the bearing capacity of the slab after steel bars yield was significantly lower than the test results. This indicates that the Cohesive model can accurately simulate the flexural properties of the composite slabs with a joint.

Fig. 17 shows the tensile damage factors of the concrete at the bottom surface of the composite slab. As presented in Fig. 17 (a), the larger tensile damage in the finite element model first occurs at the bottom interface, which was consistent with the location of the first crack in the experiment. After the loading was completed, the tensile damage distribution in the numerical model is basically consistent with the crack propagation observed in the experiment, and a large number of transverse cracks appear at the bottom of the composite slab, as depicted in Fig. 17(b). In summary, based on the comparisons between the test and analysis result, it can be concluded that the developed FEM was accurately enough to simulate the flexural performance of slab, and can be used for further study.

5. Conclusions

In this study, the flexural behaviors of composite slabs and three different forms of cast-in-situ slabs with a joint were compared, and the specimen SS-1 was taken as an example to conduct finite element analysis. the conclusions are as follow:

The failure mode of cast-in-place slabs and composite slabs with a joint in shape of T-shaped and rectangular concrete topping is that the crack width reaches the standard limit, while the failure mode of trapezoidal composite slabs is that the midspan deflection reaches the limit. Overall, all four slabs are ductile failure.

The ultimate bearing capacity of composite slabs with a joint in the shape of T-shaped and trapezoidal concrete topping are equivalent to or even higher than that of cast-in-situ slabs, and 12.9% and 19.7% higher than that of composite slab with a joint in shape of rectangular concrete topping.

According to the calculation formula for the bearing capacity of cast-in-situ slabs provided by GB50010–2010, the measured

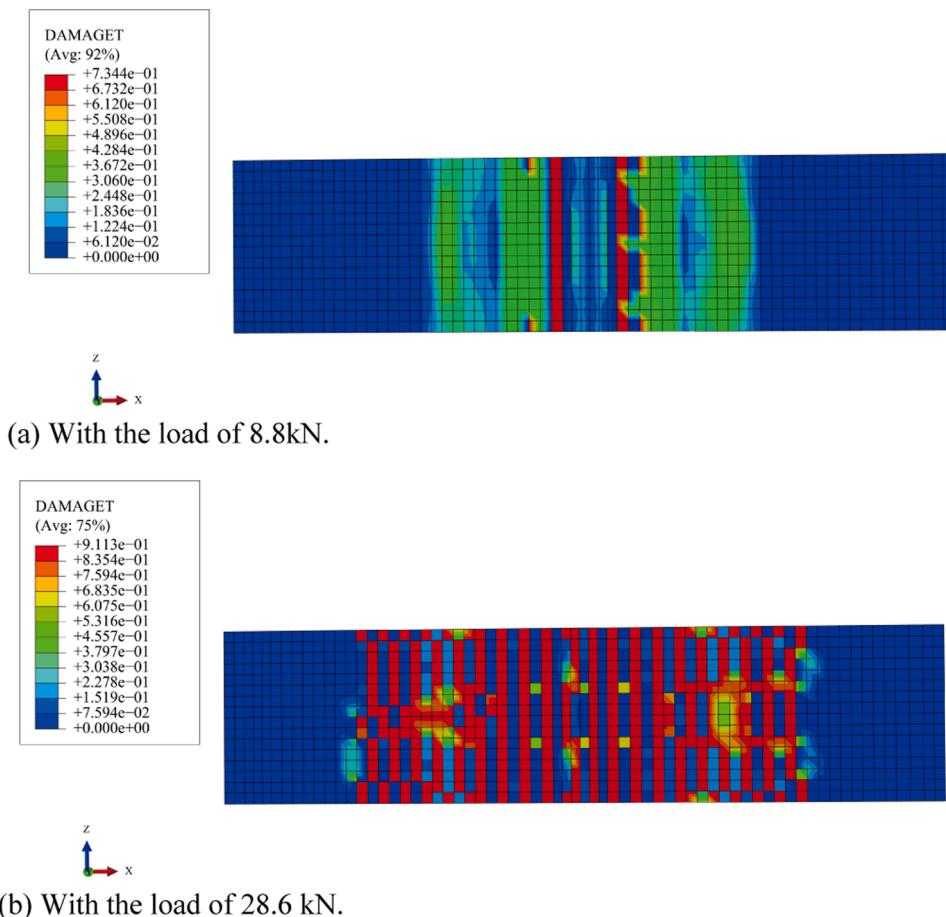


Fig. 17. The concrete tensile damage factor at the bottom surface of specimen SS-1.

bearing capacity of composite slabs was evaluated. The ratio of actual measured values to theoretical values of CS, SS-1, SS-2, and SS-3 was 1.09, 1.09, 1.16, and 0.97 respectively. The reasonable agreement indicating a good potential for the code in the design of the composite slabs with a joint in shape of T-shaped and trapezoidal concrete topping.

The cracks on the side of all composite slabs with a joint pass through the horizontal interface between the precast plank and cast-in-situ concrete topping, indicating that roughening the surface of the precast plank and bending the end of bottom longitudinal steel bars upwards can effectively transmit internal forces at the joint.

Compared to the Colum-Friction model, the Cohesive model provided by ABAQUS can accurately simulate the bending performance of the new type of composite slab with a joint, with an error of no more than 9% compared to the test results.

It should be pointed that this study did not consider the mechanical performance of the connection joints between this new type of composite slab and beam. The integrity of the slab-beam joint is another key factor determining whether this new type of composite slab can be applied in practical engineering. Therefore, further research should be conducted on the above issues.

CRedit authorship contribution statement

Lou Feng: Writing – original draft, Formal analysis, Methodology. **Chen Xiulong:** Investigation, Conceptualization, Validation. **Luo Bin:** Resources, Visualization, Writing – review & editing. **Chen Zhong:** Investigation, Visualization.

Declaration of Competing Interest

The authors declare that they have no known competing financial interests or personal relationships that could have appeared to influence the work reported in this paper.

Data availability

No data was used for the research described in the article.

Acknowledgments

This work was funded by the Huzhou city Science and Technology Plan Project (2021ZD2029).

References

- [1] X. Chong, L. Xie, X. Ye, Q. Jiang, D. Wang, Experimental study on the seismic performance of superimposed RC shear walls with enhanced horizontal joints, *J. Earthqu. Eng.* 23 (1) (2017) 1–17, <https://doi.org/10.1080/13632469.2017.1309604>.
- [2] J.G. Nie, Y.X. Jiang, X. Nie, L.D. Zhuang, Effect of truss reinforcement on mechanical properties of prefabricated slabs, *J. Build. Struct.* 42 (01) (2021) 151–158, <https://doi.org/10.14006/j.jzjgxb.2020.0007>.
- [3] X. Zhang, Z.J. Pang, S.J. Wang, D.H. Qiao, et al., Experimental study and analysis on flexural performance of free support tool-truss composite slab, *Eng. Mech.* 40 (08) (2023) 115–125, <https://doi.org/10.6052/j.issn.1000-4750.2021.12.0971>.
- [4] F.B. Wu, B. Li, J. Wen, H. Qin, et al., Experimental on new type of two-way composite floor slab with recycling truss ribs, *J. Archit. Civ. Eng.* 37 (2) (2020) 27–34, <https://doi.org/10.19815/j.jace.2019.02040>.
- [5] J.S. Zhang, Y.S. Ni, Y. Yao, Y.L. Yang, et al., Inplane mechanical property of superimposed concrete slab with precast ribbed panels jointed in different directions, *China Civ. Eng. J.* 48 (5) (2015) 23–34, <https://doi.org/10.15951/j.tmgxcb.2015.05.003>.
- [6] A. Dehghani, A. Hayatdavoodi, F. Aslani, The ultimate shear capacity of longitudinally stiffened steel-concrete composite plate girders, *J. Constr. Steel Res.* 179 (2021), <https://doi.org/10.1016/j.jcsr.2021.106550>.
- [7] H.T. Hou, M.Y. Feng, C.X. Qiu, et al., Experimental and theoretical study on flexural behavior of prestressed concrete composite slab with steel rib, *J. Build. Struct.* 39 (3) (2018) 103–110, <https://doi.org/10.14006/j.jzjgxb.2018.03.013>.
- [8] Lan Ruhai Hou Hetao, Feng Mingyuan, et al., Experimental research on flexural behavior of concrete composite slab with grouted-round-steel tube truss, *Ind. Constr.* 47 (7) (2017) 29–33, <https://doi.org/10.13204/j.gyjz201707006>.
- [9] O. Yi, J.E. Mills, Y. Zhuge, X. Ma, R.J. Gravina, O. Youssf, Performance of crumb rubber concrete composite-deck slabs in 4-point-bending, *J. Build. Eng.* 40 (2021), <https://doi.org/10.1016/j.jobe.2021.102695>.
- [10] E. Najaf, M. Orouji, K. Ghouchani, Finite element analysis of the effect of type, number, and installation angle of FRP sheets on improving the flexural strength of concrete beams, *Case Stud. Constr. Mater.* 17 (2022) 14, <https://doi.org/10.1016/j.cscm.2022.e01670>.
- [11] M. Orouji, E. Najaf, Effect of GFRP rebars and polypropylene fibers on flexural strength in high-performance concrete beams with glass powder and microsilica, *Case Stud. Constr. Mater.* 18 (2023) 11, <https://doi.org/10.1016/j.cscm.2022.e01769>.
- [12] Z.Y. Wang, Y. Wei, Y.F. Hu, et al., An investigation of the flexural performance of bamboo-concrete composite beams with precast light concrete slabs and dowel connectors, *J. Build. Eng.* 41 (2021), 102759, <https://doi.org/10.1016/j.jobe.2021.102759>.
- [13] JGJ1-2014, *Technical specification for precast concrete structures*, China Architecture and Building Press, Beijing, China, 2014.
- [14] X.G. Ye, H.G. Hua, T.S. Xu, et al., Experimental study on connection of superimposed slabs, *Ind. Constr.* 40 (01) (2010) 59–63, <https://doi.org/10.13204/j.gyjz2010.01.016>.
- [15] K.W. Ding, D. Chen, Y.L. Liu, et al., Theoretical and experimental study on mechanical behavior of laminated slabs with new type joints, *China Civ. Eng. J.* 48 (10) (2015) 64–69, <https://doi.org/10.15951/j.tmgxcb.2015.10.009>.
- [16] X.F. Zhang, S.G. Zheng, Y.C. Shan, et al., Experimental study on full-scale steel bar truss superimposed two-way slabs without extending reinforcement on all sides and connected without gap, *Build. Struct.* 49 (15) (2019) 83–87, <https://doi.org/10.19701/j.jzjg.2019.15.015>.
- [17] Y.L. Liu, J.Q. Huang, X. Chong, X.G. Ye, Experimental investigation on flexural performance of semi-precast reinforced concrete one-way slab with joint, *Struct. Concr.* 22 (4) (2021) 2243–2257, <https://doi.org/10.1002/suco.202000676>.
- [18] X. Yu, X. Li, Experimental study on bending performance of concrete composite slabs using semi-prefabricated slabs without extended bars, *Build. Struct.* 53 (05) (2023) 83–89, <https://doi.org/10.19701/j.jzjg.20201318>.
- [19] M.I.S. Mohamed, J.A. Thamboo, T. Jeyakaran, Experimental and numerical assessment of the flexural behaviour of semi-precast-reinforced concrete slabs, *Adv. Struct. Eng.* 23 (9) (2020) 1865–1879, <https://doi.org/10.1177/1369433220904011>.

- [20] S.S.E. Lam, V. Wong, R.S.M. Lee, Bonding assessment of semi-precast slabs subjected to flexural load and differential shrinkage, *Eng. Struct.* 187 (2019) 25–33, <https://doi.org/10.1016/j.engstruct.2019.02.029>.
- [21] A. Adawi, M.A. Youssef, M.E. Meshaly, Experimental investigation of the composite action between hollowcore slabs with machine-cast finish and concrete topping, *Eng. Struct.* 91 (2015) 1–15, <https://doi.org/10.1016/j.engstruct.2015.02.018>.
- [22] A. Adawi, M.A. Youssef, M.E. Meshaly, Finite element modeling of the composite action between hollowcore slabs and the topping concrete, *Eng. Struct.* 124 (2016) 302–315, <https://doi.org/10.1016/j.engstruct.2016.06.016>.
- [23] I.S. Ibrahim, K.S. Elliott, R. Abdullah, A.B.H. Kueh, N.N. Sarbini, Experimental study on the shear behaviour of precast concrete hollow core slabs with concrete topping, *Eng. Struct.* 125 (2016) 80–90, <https://doi.org/10.1016/j.engstruct.2016.06.005>.
- [24] U.A. Girhammar, M. Pajari, Tests and analysis on shear strength of composite slabs of hollow core units and concrete topping, *Constr. Build. Mater.* 22 (8) (2008) 1708–1722, <https://doi.org/10.1016/j.conbuildmat.2007.05.013>.
- [25] GB/T 228.1-2010, *Metallic materials-Tensile testing-Part 1: Method of test at room temperature*, Standards Press of China, Beijing, China, 2010.
- [26] GB/T 50081-2010, *Standard for test method of mechanical properties of ordinary concrete*, Architecture & Building Press, Beijing, China, 2010.
- [27] GB/T 50152-2012, *Standard for test method of concrete structures*, Architecture & Building Press, Beijing, China, 2012.
- [28] GB50010-2010, *Code for Design of concrete Structures*, China Architecture and Buildings Press, Beijing, China, 2010.
- [29] ABAQUS/CAE. Standard user's manual, version 6.14–1. 2014.
- [30] J.S. Zhang, Y. Yao, X.H. Zhou, Y.L. Yang, Y.Z. Wang, Failure mode and ultimate bearing capacity of precast ribbed panels used for concrete composite slabs, *Adv. Struct. Eng.* 16 (12) (2013) 2005–2017, <https://doi.org/10.1260/1369-4332.16.12.2005>.
- [31] A.S. Genikomsou, M.A. Polak, Finite element analysis of punching shear of concrete slabs using damaged plasticity model in ABAQUS, *Eng. Struct.* 98 (2015) 38–48, <https://doi.org/10.1016/j.engstruct.2015.04.016>.
- [32] F. Sidoroff, *Physic nonlinearities in structural analysis*, Springer-Verlag, Berlin, 1981.
- [33] B.Y. Deng, D. Tan, L.Z. Li, et al., Flexural behavior of precast ultra-lightweight ECC-concrete composite slab with lattice girders, *Eng. Struct.* 279 (2023), 115553, <https://doi.org/10.1016/j.engstruct.2022.115553>.
- [34] ABAQUS/CAE. Standard theory manual, version 6.14–1. 2014.
- [35] ACI 318–11. *Building code requirements for structural concrete and commentary*. American Concrete Institute. 2011.
- [36] J. Zhou, *Study on the application technology of shear walls with precast concrete hollow moulds*, Tsinghua university, Beijing, 2015.